

Dynamical Generation of Topological Magnetic Lattices for Ultracold Atoms

Jinlong Yu,^{1,3} Zhi-Fang Xu,^{2,3,*} Rong Lü,^{1,4} and Li You^{1,4}

¹*State Key Laboratory of Low Dimensional Quantum Physics,
Department of Physics, Tsinghua University, Beijing 100084, China*

²*MOE Key Laboratory of Fundamental Physical Quantities Measurements,
School of Physics, Huazhong University of Science and Technology, Wuhan 430074, China*

³*Department of Physics and Astronomy, University of Pittsburgh, Pittsburgh, Pennsylvania 15260, USA*

⁴*Collaborative Innovation Center of Quantum Matter, Beijing 100084, China*

We propose a scheme to dynamically synthesize a space-periodic effective magnetic field for neutral atoms by time-periodic magnetic field pulses. When atomic spin adiabatically follows the direction of the effective magnetic field, an adiabatic scalar potential together with a geometric vector potential emerges for the atomic center-of-mass motion, due to the Berry phase effect. While atoms hop between honeycomb lattice sites formed by the minima of the adiabatic potential, complex Peierls phase factors in the hopping coefficients are induced by the vector potential, which facilitate a topological Chern insulator. With further tuning of external parameters, both a topological phase transition and topological flat bands can be achieved, highlighting realistic prospects for studying strongly correlated phenomena in this system. Our Letter presents an alternative pathway towards creating and manipulating topological states of ultracold atoms by magnetic fields.

PACS numbers: 37.10.Gh, 67.85.-d, 81.16.Ta, 73.43.-f

Gauge fields lie at the center of our modern understanding of physics in many systems, including those of high energy and condensed matter, as well as of ultracold atoms. Within the gauge-field paradigm, interactions between particles, which enable rich quantum phases of a many-body system, are mediated through gauge fields. For instance, solid-state materials with charged quasiparticles in magnetic fields or with spin-orbit coupling (SOC) show a rich variety of quantum Hall effects and exotic topological superconductivity [1, 2]. The interplay between gauge fields and lattice systems is also of great interest (for a pedagogical review, see [3]). The spectrum of a charged particle in a square lattice exposed to a strong uniform magnetic field shows a fractal structure, widely known as the Hofstadter butterfly [4]. In another seminal work, Haldane shows that the quantum Hall effect without Landau levels can be realized when a periodically staggered magnetic field is applied to charged particles in a honeycomb lattice [5].

Ultracold atoms in lattice systems are considered to be powerful simulators for studying gauge-field physics [6–23]. Both the Hofstadter and the Haldane models with cold atoms were theoretically proposed [11–14] and experimentally demonstrated [15–21] by making use of novel forms of light-atom interactions [7], such as laser-assisted tunneling [15–18], the shaking-optical-lattice technique [21], and SOC within a synthetic dimension [19, 20]. In addition to the optical lattice formed from a space-periodic ac-Stark shift by interfering laser beams, proposals for the generation of a magnetic lattice with a space-periodic Zeeman shift have been put forth [24–32] (and some have been realized [25–28]) using current-carrying wires [24], microfabricated wires or permanent magnetic structures on atomic chips [25–30], superconducting vortex lattice shields [31], and phase imprinting by gradient magnetic pulses [32]. In contrast to optical lattices, magnetic lattices are free from atomic spontaneous emissions

that are always accompanied by heating and loss of atoms. Additionally, they have the potential to reach shorter lattice constants [30, 31] (of a few tens of nanometers as proposed in Ref. [31]), leading to improved energy scales and less stringent temperature requirements; the lattice constants can even be continuously tuned [32]. These advantageous features enhance the performance of atomic quantum gases as powerful quantum simulators.

While the simulation of gauge-field physics and the manipulation of topological states in optical lattices have shown fruitful results [6–23], it remains to show whether this is also the case for magnetic lattices. This Letter provides an affirmative first answer to this question.

This Letter presents a scheme for synthesizing a time-independent effective Hamiltonian with nontrivial band topology for atomic gases with internal spin degrees of freedom, based on the phase imprinting technique [33, 34]. A two-dimensional (2D) magnetic lattice with triangular geometry emerges in the effective Hamiltonian. In the limit when an atom is confined in the lowest Zeeman level, an adiabatic scalar potential and a geometric vector potential are simultaneously generated for the center-of-mass motion [6, 22, 23]. The adiabatic scalar potential surface can form a honeycomb lattice, while the associated geometric vector potential provides complex phases for next-nearest-neighbor (NNN) hopping coefficients in realizing the Haldane model [5, 35]. With the flexibility and tunability of magnetic fields, our scheme can be extended to produce a set of effective Hamiltonians whose lowest energy bands undertake a topological phase transition from a topological (Chern) insulator to a trivial one. Moreover, models possessing topological quasiflat bands are realized near the phase-transition point.

The protocol.—We consider a pancake-shaped quasi-2D ultracold atomic gas of spin F confined in the x - y plane (at $z = 0$). In the presence of a bias magnetic field $B_0 \hat{e}_z$, the

single-particle Hamiltonian is given by

$$H_0 = \frac{\mathbf{p}^2}{2m} + \hbar\omega_0 F_z, \quad (1)$$

where $\mathbf{p} = (p_x, p_y)$ is the 2D kinetic momentum, m is the atomic mass, \hbar is the reduced Planck constant, F_z is the third component of the atomic spin vector (in unit of \hbar) $\mathbf{F} = (F_x, F_y, F_z)$ and $\omega_0 = g_F \mu_B B_0 / \hbar$ is the Larmor frequency at B_0 , where g_F is the Landé g factor for the spin- F hyperfine state manifold and μ_B is the Bohr magneton.

A short gradient-magnetic-field pulse $B'y\hat{e}_y$ of duration $\delta t'$ imprints a space-dependent phase factor [32–34, 36–38] onto the wave function as $\exp(-ik_{so}yF_y)$, where $k_{so} = \delta t' g_F \mu_B B' / \hbar$ is the SOC strength [36, 37] with B' the magnetic gradient. After a free evolution time δt , a second magnetic field pulse in the opposite direction imprints an opposite phase. The two pulses combined together enact a unitary transformation

$$e^{ik_{so}yF_y} F_z e^{-ik_{so}yF_y} = F_z \cos(k_{so}y) - F_x \sin(k_{so}y), \quad (2)$$

which rotates the magnetic field $B_0(0,0,1)$ to a space-periodic form $B_0(-\sin(k_{so}y), 0, \cos(k_{so}y))$. Similarly, an opposite uniform-field pulse pair $\mp B_y\hat{e}_y$ with a pulse area $\delta t' g_F \mu_B B_y / \hbar = \pi$ inverts the magnetic field $B_0(0,0,1)$ to $B_0(0,0,-1)$ as $e^{-i\pi F_y} F_z e^{i\pi F_y} = -F_z$. More generally, a gradient magnetic field pulse along an arbitrary direction $\hat{e}_\theta = (\cos\theta, \sin\theta, 0)$ in the x - y plane imprints a phase factor $\exp(-ik_{so}r_\theta F_\theta)$, where $r_\theta = \mathbf{r} \cdot \hat{e}_\theta = x \cos\theta + y \sin\theta$ and $F_\theta = \mathbf{F} \cdot \hat{e}_\theta = F_x \cos\theta + F_y \sin\theta$ are, respectively, the coordinate vector $\mathbf{r} = (x, y)$ and the spin vector \mathbf{F} projected to the \hat{e}_θ direction. Following a period of free evolution and a second pulse from an opposite gradient field, an expression analogous to Eq. (2) generates a magnetic field with spatial periodicity along the \hat{e}_θ direction.

In our scheme, discussed below, repeated pulse pairs are concatenated. A complete cycle of the evolution period contains three gradient pulse pairs along directions separated by an angle of 120° , together with a $\mp\pi$ pulse pair along the y direction as shown in Fig. 1(a)–1(b). The total evolution over one complete cycle (of period $T = 4\delta t$) is then given by

$$U(T, 0) = e^{-i\pi F_y} e^{-iH_0\delta t/\hbar} e^{i\pi F_y} \times \prod_{j=3,2,1} e^{ik_{so}r_{\theta_j}F_{\theta_j}} e^{-iH_0\delta t/\hbar} e^{-ik_{so}r_{\theta_j}F_{\theta_j}}, \quad (3)$$

with $\theta_j = -\pi/6 + 2\pi j/3$. According to the Floquet theorem [40, 41], a time-independent effective Hamiltonian can be defined according to $U(T, 0) \equiv \exp(-iH_{\text{eff}}T/\hbar)$. To the lowest order of T , we find [42]

$$H_{\text{eff}} = \frac{1}{2m} \left(\mathbf{p} - \frac{3}{8} \hbar k_{so} \mathbf{F}_\perp \right)^2 + \frac{15}{64} \hbar \omega_{so} \mathbf{F}_\perp^2 + g_F \mu_B \mathbf{B}_{\text{eff}} \cdot \mathbf{F}, \quad (4)$$

where $\mathbf{F}_\perp = (F_x, F_y)$ is the 2D spin operator, $\omega_{so} = \hbar k_{so}^2 / 2m$ is the SOC frequency, and \mathbf{B}_{eff} is an effective magnetic field

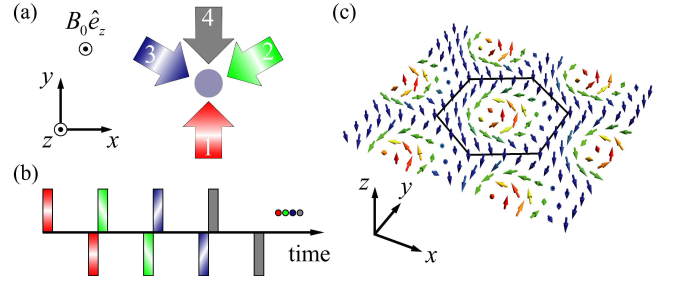


FIG. 1. A schematic illustration for synthesizing a magnetic lattice. (a) An atomic cloud is exposed to a uniform bias magnetic field $B_0\hat{e}_z$ (pointing out of the page), and subjected in sequence to four pairs of opposite magnetic pulses as shown in (b). Pulse pairs 1, 2, and 3 are gradient magnetic fields lying in the x - y plane along directions separated by 120° . Pulse pair 4 executes $\mp\pi$ spin rotations along the y direction. The color gradient represents the corresponding magnetic field strength. (b) The time-periodic pulse sequence with four pairs of pulses forms one complete evolution period. (c) A three-dimensional view of the effective magnetic field \mathbf{B}_{eff} [Eq. (5)], which forms a Skyrmion lattice [39] with its Wigner-Seitz unit cell shown by the hexagon [of edge length $4\pi/(3k_{so})$]. The arrows are colored by the magnitude of the third component of \mathbf{B}_{eff} .

whose three components are given by

$$\begin{aligned} B_{\text{eff},x} &= -\frac{B_0}{4} \sum_j \sin(k_{so}r_{\theta_j}) \sin\theta_j, \\ B_{\text{eff},y} &= \frac{B_0}{4} \sum_j \sin(k_{so}r_{\theta_j}) \cos\theta_j, \\ B_{\text{eff},z} &= \frac{B_0}{4} \left[-1 + \sum_j \cos(k_{so}r_{\theta_j}) \right]. \end{aligned} \quad (5)$$

The first two terms in Eq. (4) arise from the unitary transformations by gradient pulse pairs applied to the momentum operator [32, 36]. The third term describes a magnetic (Zeeman) lattice that couples the atomic spin to the effective magnetic field \mathbf{B}_{eff} , as shown in Fig. 1(c).

Geometric potentials and energy spectrum.—The above protocol for the generation of a triangular magnetic lattice is general, and can be applied to atoms with arbitrary spins. For concreteness, we choose a specific atomic species, fermionic ^6Li , with electron spin $J = 1/2$, nuclear spin $I = 1$, and we consider the total hyperfine spin $F = I - J = 1/2$ ground-state manifold. The Landé g factor can be evaluated according to the Breit-Rabi formula [43] to be $g_F \approx -1/3$. The spin operator reduces to $\mathbf{F} = \boldsymbol{\sigma}/2$, where $\boldsymbol{\sigma}$ is the vector of Pauli matrices. To be more specific, in all numerical calculations, we assume a set of fixed parameters unless otherwise noted. They are $B_0 = 20$ mG, $B'\delta t' = 2$ G cm $^{-1}$ ms [44], which correspond to $k_{so} = (1.7 \mu\text{m})^{-1}$ and $\omega_0 = 32.3\omega_{so} = (2\pi) \times 9.3$ kHz for the $F = 1/2$ manifold of ^6Li . With these parameters, the lattice term in Eq. (4) dominates during time evolution.

We denote the space-dependent eigenstates of the magnetic lattice by $|\chi_{1,2}(\mathbf{r})\rangle$, which satisfy

$$g_F \mu_B \mathbf{B}_{\text{eff}} \cdot \frac{\boldsymbol{\sigma}}{2} |\chi_{1,2}(\mathbf{r})\rangle = \pm \epsilon_0(\mathbf{r}) |\chi_{1,2}(\mathbf{r})\rangle, \quad (6)$$

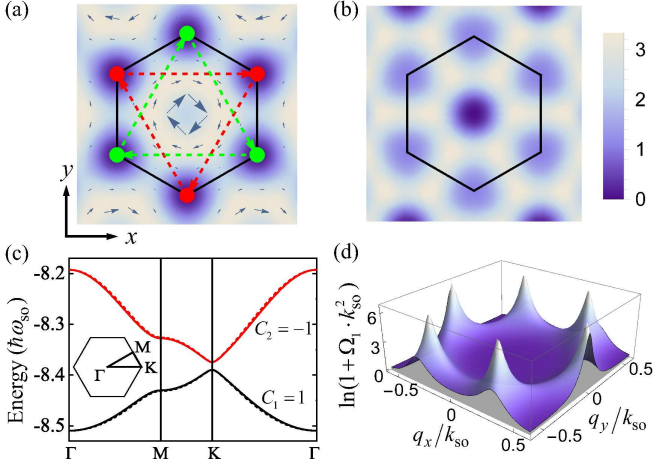


FIG. 2. Mapping the effective Hamiltonian [Eq. (4)] to the Haldane model. (a) The density plot of the adiabatic potential ϵ_0 (in blue) and its associated vector potential \mathbf{A} shown by field of arrows. A darker color denotes a smaller ϵ_0 , the minima of which form a honeycomb lattice with two sites per unit cell denoted, respectively, by red and green filled circles. The dashed lines denote NNN hopping paths along the directions of positive Peierls phases. (b) The flux density n_ϕ , in units of $10^{-2}k_{so}^2$. The hexagons in (a) and (b) denote the primitive unit cell [the same as in Fig. 1(c)], over which the net flux is unity. (c) Energy spectrum. Solid lines represent the lowest two energy bands along lines with high symmetry in the first Brillouin zone (inserted hexagon) for the effective Hamiltonian Eq. (4), with $\omega_0 = 32.3\omega_{so}$. Dashed lines represent the fitted band structure using the Haldane model results. The edge length of the inserted hexagon is $k_{so}/\sqrt{3}$. (d) A logarithmic plot of the Berry curvature for the lowest band Ω_1 . The integration of Ω_1 in the first Brillouin zone gives its Chern number, $C_1 = 1$.

where $\epsilon_0(\mathbf{r}) = -|g_F\mu_B\mathbf{B}_{\text{eff}}|/2$ is the adiabatic potential for atomic center-of-mass motion in the lower-energy eigenstate $|\chi_1\rangle$. For an atom adiabatically moving in this space-periodic Zeeman level, a vector potential $\mathbf{A}(\mathbf{r})$ emerges [42, 45],

$$\mathbf{A} = i\hbar \langle \chi_1 | \nabla | \chi_1 \rangle + \frac{3}{16} \hbar k_{so} \langle \chi_1 | \boldsymbol{\sigma}_\perp | \chi_1 \rangle, \quad (7)$$

with $\boldsymbol{\sigma}_\perp = (\sigma_x, \sigma_y)$. Associated with the vector potential is the flux density $n_\phi = (\nabla \times \mathbf{A})_z / 2\pi\hbar$, which shares the same spatial periodicity as \mathbf{B}_{eff} and can be considered in general as a type of flux lattice [22].

The adiabatic potential ϵ_0 , vector potential \mathbf{A} , and the flux density n_ϕ for our magnetic lattice are shown in Figs. 2(a) and 2(b) [46]. As shown in Fig. 2(a), the local minima of ϵ_0 are located at the corners of the unit cell, forming a honeycomb lattice. When an atom hops between these honeycomb sites, the vector potential contributes a complex Peierls phase factor $\exp(i \int \mathbf{A} \cdot d\mathbf{l}/\hbar)$ to the hopping coefficient [4, 5, 35], with the integration evaluated along the corresponding hopping path. As \mathbf{A} vanishes along the edges of the hexagon, the nearest-neighboring (NN) phase factor is a trivial unity. While along the NNN hopping paths [dashed lines in Fig. 2(a)], the accumulated phases are always nonzero. Thus the adiabatic scalar potential together with the geometric vector potential

realizes the Haldane model in the tight-binding limit. As a caveat, our flux pattern shown in Fig. 2(b) is not the same as that suggested by Haldane [5], where the staggered flux density gives a vanishing net flux over a unit cell. The flux distribution shown in Fig. 2(b) is non-negative everywhere, and the net flux over one unit cell is unity rather than zero; this can be checked by integrating the following over a unit cell: $N_\phi = \frac{1}{4\pi} \int_{\text{UC}} dx dy (\mathbf{m} \cdot \partial_x \mathbf{m} \times \partial_y \mathbf{m})$, with $\mathbf{m} = \mathbf{B}_{\text{eff}}/|\mathbf{B}_{\text{eff}}|$ [22]. Thus, the nontrivial winding pattern of \mathbf{B}_{eff} shown in Fig. 1(c) leads to a quantized net flux $N_\phi = 1$. A nonzero net flux generally leads to larger Peierls phases (of order unity). It also facilitates simulation of charged particles in strong magnetic field with nondispersive Landau levels [22, 47].

To quantitatively confirm that our model indeed maps onto the Haldane model, we numerically study the spectrum and Berry curvature [48] of the effective Hamiltonian Eq. (4) using the plane-wave expansion method [42, 49]. The typical band structure and the Berry curvature for the lowest band are shown, respectively, in Figs. 2(c) and 2(d). A band gap opens at the corners of the first Brillouin zone ($\pm K$ points), where the Berry curvature is at a maximum. Both the eigenenergies and the Berry curvatures are even functions of quasimomentum, so the spectrum at $K' = -K$ is not shown. The Chern numbers [50] for the lowest two bands are $C_{1,2} = \pm 1$, respectively. The spectrum and the Berry curvature thus resemble the ones from the Haldane model. To further validate this correspondence, we adopt the method used in Ref. [51] to get the NN hopping constant t_1 and the complex NNN hopping constant $|t_2|e^{i\phi}$ of the Haldane model from the calculated band structure. We find $t_1 = 0.053\hbar\omega_{so}$ and $|t_2| = 0.0037\hbar\omega_{so}$ with $\phi = 0.40$. Using these three parameters together with an overall energy shift, the tight-binding band structure of the Haldane model is plotted with dashed lines in Fig. 2(c).

Topological phase transition and quasiflat bands.—Our protocol allows for the easy tuning of two parameters: the SOC strength $k_{so} = \delta t' g_F \mu_B B' / \hbar$ and the bias magnetic field B_0 . Both can be tuned continuously, and can be turned on adiabatically to reach the ground state for our model system Eq. (4) [8, 21] (see [42] for details). Once the ground state is achieved, we can apply an additional weak optical gradient field (which commutes with all the pulse manipulation operations) in the x - y plane to drive Bloch oscillations and then measure the perpendicular center-of-mass drift to extract the topological properties for the lowest energy band [17, 21, 52]. With unequal durations between subsequent pulse pairs, or allowing for specific k_{so} and B_0 values for different subperiods, several variants of the effective Hamiltonian can be synthesized. A topological phase transition for the lowest energy band can be achieved by a simple tuning of the bias magnetic field. For this to occur, we set the field strength to be B_0 for the first three subperiods and switch to αB_0 for the fourth subperiod; our protocol then leads to a change for the z component of the effective magnetic field in Eq. (5) as

$$B_{\text{eff},z} = \frac{B_0}{4} \left[-\alpha + \sum_j \cos(k_{so} r_{\theta_j}) \right]. \quad (8)$$

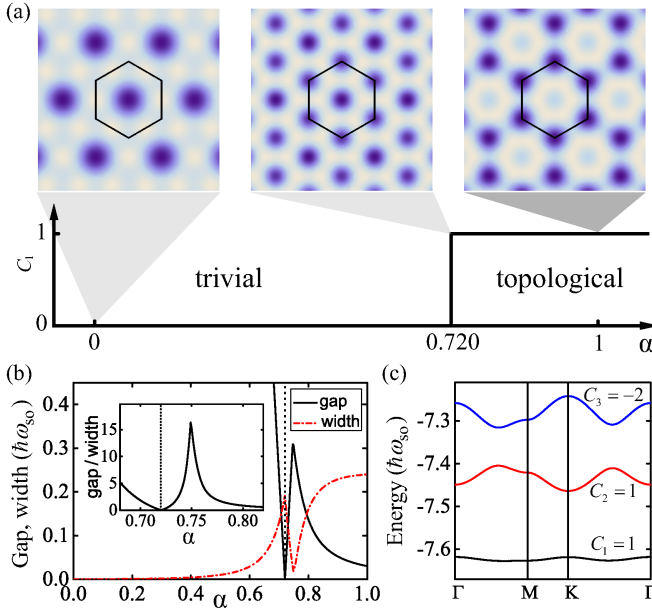


FIG. 3. Illustration of the structural and topological phase transition with the tuning of the z component of \mathbf{B}_{eff} in Eq. (8). (a) Top panel: the density plots of the adiabatic potentials for $\alpha = 0$ (left), $\alpha = 0.720$ (middle), and $\alpha = 1$ (right) with the minima (dark colors) forming a simple triangular lattice, a decorated triangular lattice, and a honeycomb lattice, respectively. Bottom panel: The Chern number for the lowest energy band as a function of α . A topological phase transition occurs at the critical point of $\alpha = 0.720$. (b) The band gap between the lowest two bands and the band width for the lowest band, as a function of α . The band gap closes at $\alpha = 0.720$ (marked by the dotted vertical line). The inset shows the dependence of the band gap-over-width ratio on α . It peaks at $\alpha = 0.749$ with a value of 16. (c) The lowest three bands at $\alpha = 0.749$.

The $\alpha = 1$ case corresponds to the original proposal with topological bands, while the $\alpha = 0$ case describes a system of trivial energy bands with zero Chern numbers. By continuously tuning α from 0 to 1, a topological phase transition with band touching and reopening takes place, as summarized in Fig. 3.

Figure 3(a) presents the changing Chern number and, hence, the band topology, for the lowest band with increasing α . The lattice geometry of the adiabatic potential is found to undergo a structural transformation first from a simple triangular lattice to a decorated triangular lattice [53], and then to a honeycomb lattice. The corresponding tight-binding descriptions for s orbitals involve 1, 3, and 2 bands, respectively, for the three cases. As α increases, the band originating from hopping between s orbitals located at unit cell centers crosses the two bands from s orbitals located at the corners. Their corresponding Chern numbers change after band touching and reopening. Figure 3(b) shows the behavior of the gap between the lowest two bands as well as the band width for the lowest one. Gap closing occurs at the Γ point when $\alpha = 0.720$, and the gap-over-width ratio is found to be quite large over a limited range after a gap opening with a peak value as large as 16 when $\alpha = 0.749$, as shown in the inset of Fig. 3(b). The energy

spectrum at $\alpha = 0.749$ is shown in Fig. 3(c). The lowest band is a Landau-level-like topological quasiflat one [54]. Such a nondispersive topological band also persists beyond the adiabatic limit [42]. It is a promising candidate for simulating the fractional quantum Hall effect when suitable interactions are included [55–58]. It is perhaps worth pointing out, also, that a flat band can emerge as the second excited band in a Kagome lattice [53], or as the first excited band in a Lieb lattice [59]. The properties of the localized states in the flat band of a Lieb lattice have been investigated in a recent experiment [59].

We focus in this Letter on discussing single-particle physics of a fermionic spin-1/2 system, though our magnetic lattice generation protocol can be equally applied to a higher-spin atom, be it a boson or fermion. When local momentum-independent (s wave) interaction is taken into account, it can be simply added to the effective Hamiltonian because it commutes with all the pulse manipulation operations (see also [36, 37]). The topological phase is expected to be stable for weak interactions due to the presence of a gap. However, stronger interaction can drive the system to new phases, in which the physics may be dominated by the interplay between the correlation and band topology. A detailed study of the interaction effects for this system deserves further efforts.

In conclusion, we propose an experimentally feasible protocol to realize a synthetic magnetic field with real magnetic field pulses. The synthetic magnetic field forms a lattice with nontrivial band topology, and under certain limits can be mapped to the Haldane model. The high tunability of our scheme makes it possible to design a topological phase transition as well as quasiflat energy bands with nontrivial topology, which could push the effective model into the strongly correlated regime.

We thank Professors W. Vincent Liu and Kun Yang for valuable discussions. This work is supported by the MOST Grant No. 2013CB922004 of the National Key Basic Research Program of China and by the NSFC (Grants No. 91121005, No. 91421305, and No. 11374176), as well as by U.S. AFOSR (Grant No. FA9550-12-1-0079), ARO (Grant No. W911NF-11-1-0230), the Charles E. Kaufman Foundation, and the Pittsburgh Foundation (J.Y. and Z.-F. X.). R.L. also wants to acknowledge support from the NSFC (Grant No. 11274195).

* zfxu83@gmail.com

- [1] M. Z. Hasan and C. L. Kane, *Rev. Mod. Phys.* **82**, 3045 (2010).
- [2] X.-L. Qi and S.-C. Zhang, *Rev. Mod. Phys.* **83**, 1057 (2011).
- [3] B. A. Bernevig and T. L. Hughes, *Topological Insulators and Topological Superconductors* (Princeton University Press, Princeton, NJ, 2013).
- [4] D. R. Hofstadter, *Phys. Rev. B* **14**, 2239 (1976).
- [5] F. D. M. Haldane, *Phys. Rev. Lett.* **61**, 2015 (1988).
- [6] J. Dalibard, F. Gerbier, G. Juzeliūnas, and P. Öhberg, *Rev. Mod. Phys.* **83**, 1523 (2011).
- [7] N. Goldman, G. Juzeliūnas, P. Öhberg, and I. B. Spielman,

- Rep. Prog. Phys. **77**, 126401 (2014).
- [8] N. Goldman and J. Dalibard, *Phys. Rev. X* **4**, 031027 (2014).
- [9] J. Struck, C. Ölschläger, R. Le Targat, P. Soltan-Panahi, A. Eckardt, M. Lewenstein, P. Windpassinger, and K. Sengstock, *Science* **333**, 996 (2011).
- [10] P. Hauke, O. Tieleman, A. Celi, C. Ölschläger, J. Simonet, J. Struck, M. Weinberg, P. Windpassinger, K. Sengstock, M. Lewenstein, and A. Eckardt, *Phys. Rev. Lett.* **109**, 145301 (2012).
- [11] D. Jaksch and P. Zoller, *New J. Phys.* **5**, 56 (2003).
- [12] A. Celi, P. Massignan, J. Ruseckas, N. Goldman, I. B. Spielman, G. Juzeliūnas, and M. Lewenstein, *Phys. Rev. Lett.* **112**, 043001 (2014).
- [13] A. G. Grushin, A. Gómez-León, and T. Neupert, *Phys. Rev. Lett.* **112**, 156801 (2014).
- [14] W. Zheng and H. Zhai, *Phys. Rev. A* **89**, 061603 (2014).
- [15] M. Aidelsburger, M. Atala, M. Lohse, J. T. Barreiro, B. Paredes, and I. Bloch, *Phys. Rev. Lett.* **111**, 185301 (2013).
- [16] H. Miyake, G. A. Siviloglou, C. J. Kennedy, W. C. Burton, and W. Ketterle, *Phys. Rev. Lett.* **111**, 185302 (2013).
- [17] M. Aidelsburger, M. Lohse, C. Schweizer, M. Atala, J. T. Barreiro, S. Nascimbene, N. R. Cooper, I. Bloch, and N. Goldman, *Nat. Phys.* **11**, 162 (2015).
- [18] C. J. Kennedy, W. C. Burton, W. C. Chung, and W. Ketterle, *Nat. Phys.* **11**, 859 (2015).
- [19] M. Mancini, G. Pagano, G. Cappellini, L. Livì, M. Rider, J. Catani, C. Sias, P. Zoller, M. Inguscio, M. Dalmonte, and L. Fallani, *Science* **349**, 1510 (2015).
- [20] B. K. Stuhl, H.-I. Lu, L. M. Ayccock, D. Genkina, and I. B. Spielman, *Science* **349**, 1514 (2015).
- [21] G. Jotzu, M. Messer, R. Desbuquois, M. Lebrat, T. Uehlinger, D. Greif, and T. Esslinger, *Nature (London)* **515**, 237 (2014).
- [22] N. R. Cooper, *Phys. Rev. Lett.* **106**, 175301 (2011).
- [23] K. Jimenez-Garcia, L. J. LeBlanc, R. A. Williams, M. C. Beeler, A. R. Perry, and I. B. Spielman, *Phys. Rev. Lett.* **108**, 225303 (2012).
- [24] J. Yin, W. Gao, J. Hu, and Y. Wang, *Opt. Commun.* **206**, 99 (2002).
- [25] A. Günther, S. Kraft, M. Kemmler, D. Koelle, R. Kleiner, C. Zimmermann, and J. Fortágh, *Phys. Rev. Lett.* **95**, 170405 (2005).
- [26] M. Singh, M. Volk, A. Akulshin, A. Sidorov, R. McLean, and P. Hannaford, *J. Phys. B* **41**, 065301 (2008).
- [27] S. Whitlock, R. Gerritsma, T. Fernholz, and R. J. C. Spreeuw, *New J. Phys.* **11**, 023021 (2009).
- [28] S. Jose, P. Surendran, Y. Wang, I. Herrera, L. Krzemien, S. Whitlock, R. McLean, A. Sidorov, and P. Hannaford, *Phys. Rev. A* **89**, 051602 (2014).
- [29] A. Grabowski and T. Pfau, *Eur. Phys. J. D* **22**, 347 (2003).
- [30] V. Leung, A. Tauschinsky, N. van Druten, and R. Spreeuw, *Quantum Inf. Process.* **10**, 955 (2011).
- [31] O. Romero-Isart, C. Navau, A. Sanchez, P. Zoller, and J. I. Cirac, *Phys. Rev. Lett.* **111**, 145304 (2013).
- [32] X. Luo, L. Wu, J. Chen, R. Lu, R. Wang, and L. You, *New J. Phys.* **17**, 083048 (2015).
- [33] S. Burger, K. Bongs, S. Dettmer, W. Ertmer, K. Sengstock, A. Sanpera, G. V. Shlyapnikov, and M. Lewenstein, *Phys. Rev. Lett.* **83**, 5198 (1999).
- [34] J. Denschlag, J. E. Simsarian, D. L. Feder, C. W. Clark, L. A. Collins, J. Cubizolles, L. Deng, E. W. Hagley, K. Helmerson, W. P. Reinhardt, S. L. Rolston, B. I. Schneider, and W. D. Phillips, *Science* **287**, 97 (2000).
- [35] L. B. Shao, S.-L. Zhu, L. Sheng, D. Y. Xing, and Z. D. Wang, *Phys. Rev. Lett.* **101**, 246810 (2008).
- [36] Z.-F. Xu, L. You, and M. Ueda, *Phys. Rev. A* **87**, 063634 (2013).
- [37] B. M. Anderson, I. B. Spielman, and G. Juzeliūnas, *Phys. Rev. Lett.* **111**, 125301 (2013).
- [38] X. Luo, L. Wu, J. Chen, Q. Guan, K. Gao, Z.-F. Xu, L. You, and R. Wang, *Sci. Rep.* **6**, 18983 (2016).
- [39] N. Nagaosa and Y. Tokura, *Nat. Nanotechnol.* **8**, 899 (2013).
- [40] M. M. Maricq, *Phys. Rev. B* **25**, 6622 (1982).
- [41] C. P. Slichter, *Principles of Magnetic Resonance*, 3rd ed. (Springer-Verlag, New York, 1990).
- [42] See Supplemental Material for details on the derivation of effective Hamiltonian, the numerical methods employed for the energy spectrum and Berry curvature, the validity of the effective Hamiltonian, the reduction of the artificial gauge fields, the energy spectrum beyond the limit of adiabatic approximation, and the adiabatic preparation of the ground state.
- [43] G. K. Woodgate, *Elementary Atomic Structure*, 2nd ed. (Oxford University Press, Oxford, 1980).
- [44] A magnetic gradient pulse with B' as large as 400 kG cm^{-1} and duration $\delta t'$ less than $1 \mu\text{s}$ is achievable in state-of-the-art atomic chip experiments; see for example S. Machluf, Y. Japha, and R. Folman, *Nat. Commun.* **4**, 2424 (2013).
- [45] A geometric scalar potential $W(\mathbf{r})$ also emerges along with the vector potential; its contribution to the total scalar potential is negligibly small compared to the adiabatic potential in the adiabatic limit [42].
- [46] The vector potential \mathbf{A} contains a gauge-dependent singularity, which is chosen to be at the center of the unit cell for the gauge we use.
- [47] N. R. Cooper and J. Dalibard, *Europhys. Lett.* **95**, 66004 (2011).
- [48] D. Xiao, M.-C. Chang, and Q. Niu, *Rev. Mod. Phys.* **82**, 1959 (2010).
- [49] N. W. Ashcroft and N. D. Mermin, *Solid State Physics* (Cengage Learning, New York, 1976).
- [50] D. J. Thouless, M. Kohmoto, M. P. Nightingale, and M. den Nijs, *Phys. Rev. Lett.* **49**, 405 (1982).
- [51] J. Ibanez-Azpiroz, A. Eiguren, A. Bergara, G. Pettini, and M. Modugno, *Phys. Rev. A* **90**, 033609 (2014).
- [52] A. Dauphin and N. Goldman, *Phys. Rev. Lett.* **111**, 135302 (2013).
- [53] G.-B. Jo, J. Guzman, C. K. Thomas, P. Hosur, A. Vishwanath, and D. M. Stamper-Kurn, *Phys. Rev. Lett.* **108**, 045305 (2012).
- [54] A. S. Sørensen, E. Demler, and M. D. Lukin, *Phys. Rev. Lett.* **94**, 086803 (2005).
- [55] S. Yang, Z.-C. Gu, K. Sun, and S. Das Sarma, *Phys. Rev. B* **86**, 241112 (2012).
- [56] S. A. Parameswaran, R. Roy, and S. L. Sondhi, *C. R. Phys.* **14**, 816 (2013).
- [57] N. R. Cooper and J. Dalibard, *Phys. Rev. Lett.* **110**, 185301 (2013).
- [58] E. J. Bergholtz and Z. Liu, *Int. J. Mod. Phys. B* **27**, 1330017 (2013).
- [59] S. Taie, H. Ozawa, T. Ichinose, T. Nishio, S. Nakajima, and Y. Takahashi, *Sci. Adv.* **1**, e1500854 (2015).

Supplemental Material for: Dynamical Generation of Topological Magnetic Lattices for Ultracold Atoms

Jinlong Yu^{1,3}, Zhi-Fang Xu^{2,3}, Rong Lü^{1,4}, and Li You^{1,4}

¹State Key Laboratory of Low Dimensional Quantum Physics,
Department of Physics, Tsinghua University, Beijing 100084, China

²MOE Key Laboratory of Fundamental Physical Quantities Measurements,
School of Physics, Huazhong University of Science and Technology, Wuhan 430074, China

³Department of Physics and Astronomy, University of Pittsburgh, Pittsburgh, Pennsylvania 15260, USA

⁴Collaborative Innovation Center of Quantum Matter, Beijing 100084, China

This supplementary material provides more details for the various points mentioned in the main article.

Derivation of the effective Hamiltonian

As explained in the main text, a gradient magnetic field pulse along $\hat{e}_\theta = (\cos \theta, \sin \theta, 0)$ in the x - y plane prints a phase factor $\exp(-ik_{\text{so}}r_\theta F_\theta)$ onto the single particle wave function. Under the action of an opposite pulse pair, the atomic momentum $\mathbf{p} = \hbar\mathbf{k}$ and spin F_z transform according to,

$$\begin{aligned} e^{ik_{\text{so}}r_\theta F_\theta} k_x e^{-ik_{\text{so}}r_\theta F_\theta} &= k_x - k_{\text{so}}F_\theta \cos \theta, \\ e^{ik_{\text{so}}r_\theta F_\theta} k_y e^{-ik_{\text{so}}r_\theta F_\theta} &= k_y - k_{\text{so}}F_\theta \sin \theta, \\ e^{ik_{\text{so}}r_\theta F_\theta} F_z e^{-ik_{\text{so}}r_\theta F_\theta} &= F_z \cos(k_{\text{so}}r_\theta) - \tilde{F}_\theta \sin(k_{\text{so}}r_\theta), \end{aligned} \quad (\text{S1})$$

where $\tilde{F}_\theta \equiv F_x \sin \theta - F_y \cos \theta$ is the spin operator perpendicular to \hat{e}_θ . Thus the evolution including the pulse pair gives rise to

$$U_\theta(\delta t, 0) = e^{ik_{\text{so}}r_\theta F_\theta} e^{-iH_0\delta t/\hbar} e^{-ik_{\text{so}}r_\theta F_\theta} \equiv e^{-iH_\theta\delta t/\hbar}, \quad (\text{S2})$$

with the corresponding Hamiltonian

$$\begin{aligned} H_\theta &= e^{ik_{\text{so}}r_\theta F_\theta} H_0 e^{-ik_{\text{so}}r_\theta F_\theta} \\ &= \frac{\hbar^2}{2m} (k_x - k_{\text{so}}F_\theta \cos \theta)^2 + \frac{\hbar^2}{2m} (k_y - k_{\text{so}}F_\theta \sin \theta)^2 \\ &\quad + \hbar\omega_0 [F_z \cos(k_{\text{so}}r_\theta) - \tilde{F}_\theta \sin(k_{\text{so}}r_\theta)]. \end{aligned} \quad (\text{S3})$$

A $\mp\pi$ pulse pair along the y direction flips the direction of the magnetic field seen by atom without inducing coupling to momentum. The evolution operator from such a pulse pair is given by

$$U_{y,\pi}(\delta t, 0) = e^{-i\pi F_y} e^{-iH_0\delta t/\hbar} e^{i\pi F_y} \equiv e^{-iH_{y,\pi}\delta t/\hbar}, \quad (\text{S4})$$

with the corresponding Hamiltonian

$$H_{y,\pi} = \frac{\hbar^2}{2m} (k_x^2 + k_y^2) - \hbar\omega_0 F_z. \quad (\text{S5})$$

A complete evolution period contains three gradient pulse pairs separated by a mutual angle of 120° in the x - y plane, together with a $\mp\pi$ pulse pair along the y direction, the corresponding evolution operator for one period $T = 4\delta t$ is given by

$$\begin{aligned} U(T = 4\delta t, 0) &= e^{-iH_{y,\pi}\delta t/\hbar} e^{-iH_{\theta_3}\delta t/\hbar} e^{-iH_{\theta_2}\delta t/\hbar} e^{-iH_{\theta_1}\delta t/\hbar} \\ &\equiv e^{-iH_{\text{eff}}T/\hbar}, \end{aligned} \quad (\text{S6})$$

with $\theta_j = -\frac{\pi}{6} + \frac{2\pi j}{3}$. We use H_m to denote the Hamiltonian for each subperiods as

$$H_1 = H_{\theta_1}, H_2 = H_{\theta_2}, H_3 = H_{\theta_3}, H_4 = H_{y,\pi}. \quad (\text{S7})$$

To lowest order of the Trotter's expansion for T , the effective Hamiltonian H_{eff} is the average of H_m ,

$$H_{\text{eff}} = \frac{1}{N} \sum_{m=1}^N H_m, \quad (\text{S8})$$

with $N = 4$ for the current case. Expanding out the terms in this Hamiltonian explicitly, we arrive at the effective Hamiltonian as shown in the main text after recombining them.

The higher order corrections of the effective Hamiltonian can also be derived through the Magnus expansion method, which to first order of T gives [41]

$$H_{\text{eff}} = \frac{1}{N} \sum_{m=1}^N H_m + \frac{iT}{2\hbar N^2} \sum_{m<n=2}^N [H_m, H_n]. \quad (\text{S9})$$

From Eq. (S6) we see that, our protocol can also be viewed as a periodically driven 4-step sequence, where the dynamics of the driven system can be understood in terms of the effective Hamiltonian and the associated micromotion [8]. We now provide the details for how our system fits into this formulism. The Hamiltonian for a general N-step sequence is described by $H_m = H^{(0)} + V_m$, with the constraint $\sum_{m=1}^N V_m = 0$. Thus we find

$$H^{(0)} = \frac{1}{N} \sum_{m=1}^N H_m, \quad (\text{S10})$$

which is just the time-averaged effective Hamiltonian Eq. (S8), and correspondingly

$$V_m = H_m - \frac{1}{N} \sum_{m=1}^N H_m. \quad (\text{S11})$$

The evolution operator for such a driven system can be partitioned in the following as introduced in Ref. [8]

$$U(t, 0) = e^{-iK(t)} e^{-it\tilde{H}_{\text{eff}}/\hbar} e^{iK(0)}, \quad (\text{S12})$$

where the effective Hamiltonian \tilde{H}_{eff} and the initial-kick operator $K(0)$ of the N-step sequence to first order of T are given by [8]

$$\begin{aligned} \tilde{H}_{\text{eff}} &= H^{(0)} + H^{(1)} = H^{(0)} + \frac{iT}{N^3} \sum_{m<n=2}^N C_{m,n} [V_m, V_n], \\ K(0) &= \frac{T}{N^2 \hbar} \sum_{m=1}^N V_m m, \end{aligned} \quad (\text{S13})$$

with $C_{m,n} = \frac{N}{2} + m - n$. For a full evolution cycle ($t = T$), the evolution operator is found to be

$$U(T, 0) = e^{-iK(T)} e^{-iT\tilde{H}_{\text{eff}}/\hbar} e^{iK(0)} = e^{-iT H_{\text{eff}}/\hbar}, \quad (\text{S14})$$

where the Hamiltonian H_{eff} to first order of T is given by [using $K(T) = K(0)$]

$$H_{\text{eff}} = e^{-iK(T)} \tilde{H}_{\text{eff}} e^{iK(0)} \simeq H^{(0)} + H^{(1)} - i[K(0), H^{(0)}]. \quad (\text{S15})$$

Inserting Eqs. (S10), (S11) and (S13) into the above equation, we recover Eq. (S9) as expected.

This shows that, the micromotion of the N-step periodically driven system gives the first order correction to the effective Hamiltonian. This calls for the use of the time-averaged effective Hamiltonian Eq. (S8) to approximate the evolution in the short T limit. This approximation will be validated numerically in the later sections.

Solving the effective Hamiltonian with the plane wave expansion method

For spin-1/2 with $\mathbf{F} = \sigma/2$, the effective Hamiltonian takes the following form

$$H_{\text{eff}} = \frac{1}{2m} \left(\mathbf{p} - \frac{3}{16} \hbar k_{\text{so}} \sigma_{\perp} \right)^2 + \frac{1}{2} g_F \mu_B \mathbf{B}_{\text{eff}} \cdot \sigma, \quad (\text{S16})$$

with $\sigma_{\perp} = (\sigma_x, \sigma_y)$ after omitting a constant energy shift $15\hbar\omega_{\text{so}}/128$. As H_{eff} in Eq. (S16) is space-periodic, its eigenstates can be labeled with quasimomentum $\mathbf{q} = (q_x, q_y)$ in the first Brillouin zone as good quantum numbers. Expanded in the plane wave basis [49], the eigenstates take the form

$$\psi_{n\mathbf{q}}(\mathbf{r}) = e^{i\mathbf{q}\cdot\mathbf{r}} \sum_{l,m} e^{i(l\mathbf{b}_1 + m\mathbf{b}_2)\cdot\mathbf{r}} \begin{pmatrix} C_{l,m,\uparrow} \\ C_{l,m,\downarrow} \end{pmatrix}, \quad (\text{S17})$$

where n is the band index, $\mathbf{b}_{1,2} = k_{so} \left(\mp \cos\left(\frac{\pi}{6}\right), -\sin\left(\frac{\pi}{6}\right) \right)$ are the two reciprocal unit vectors, l, m are integers taking values $0, \pm 1, \pm 2$, etc. The expansion coefficients $C_{l,m,\uparrow(\downarrow)}$ are to be determined. The plane wave expansion Eq. (S17) together with the eigenvalue equation

$$H_{\text{eff}} \psi_{n\mathbf{q}}(\mathbf{r}) = E_n(\mathbf{q}) \psi_{n\mathbf{q}}(\mathbf{r}), \quad (\text{S18})$$

determines the energy spectrum, as well as the Bloch wave functions as eigenfunctions.

In our numerical calculations, we use a cutoff $N = 15$ as the maximal value for $|l|$ and $|m|$. And we have checked that, for $N > 10$ cases, the band structures shown in the main text are independent of the choice of N . Thus in the plane wave basis, the Hamiltonian is expressed as a $[2(2N+1)^2] \times [2(2N+1)^2]$ matrix for each quasimomentum \mathbf{q} within the first Brillouin zone. The eigenvalues and corresponding eigenvectors give respectively the energy spectrum and Bloch wave functions.

Once the Bloch wave functions are obtained, we can calculate their Berry curvatures $\Omega_n(\mathbf{q})$ and (first) Chern numbers C_n for each energy bands according to [48]

$$\begin{aligned} \Omega_n(\mathbf{q}) &= i \left[\nabla_{\mathbf{q}} \times \langle u_n(\mathbf{q}) | \nabla_{\mathbf{q}} | u_n(\mathbf{q}) \rangle \right]_z, \\ C_n &= \frac{1}{2\pi} \int_{\text{BZ}} d^2q \Omega_n(\mathbf{q}), \end{aligned} \quad (\text{S19})$$

where $u_{n\mathbf{q}}(\mathbf{r}) = \langle \mathbf{r} | u_n(\mathbf{q}) \rangle = e^{-i\mathbf{q}\cdot\mathbf{r}} \psi_{n\mathbf{q}}(\mathbf{r})$ is the cell-periodic part of the Bloch function.

Validity of the effective Hamiltonian

We use the effective Hamiltonian to describe the evolution of ultracold atoms under the magnetic field pulse sequence of the proposed protocol. The use of Trotter expansion limits its validity to short evolution periods. In this subsection we use two complimentary methods to check for this approximation.

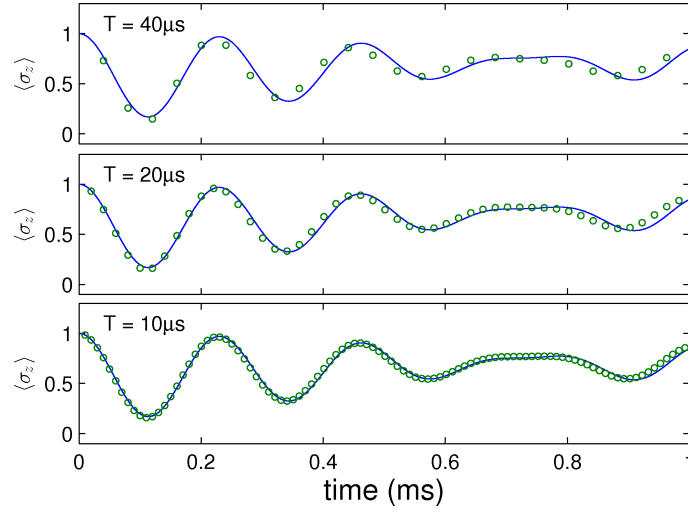


FIG. S1. The evolution of a Gaussian wave packet located at the center of a harmonic trap, with oscillator frequencies $\omega_x = \omega_y = (2\pi) \times 30$ Hz is investigated. The system is initially prepared in the spin up state. The figure shows the time dependent population imbalance $\langle \sigma_z \rangle$ calculated from the effective Hamiltonian (solid line), and the actual pulse sequence (open circles), with evolution periods $T = 40 \mu\text{s}$, $20 \mu\text{s}$, and $10 \mu\text{s}$, from top to down respectively. The other parameters are $\omega_0 = 32.3\omega_{so} = (2\pi) \times 9.3$ kHz, $\alpha = 1$.

The first method relies on evolving an eigenstate, whereby the initial state $\psi_{n\mathbf{q}}(\mathbf{r}, t = 0)$ is prepared in an eigenstate of the effective Hamiltonian with a given band index n and quasimomentum \mathbf{q} . The actual magnetic field pulse sequence is then used to evolve it to a later time $t > 0$ where the wave function is denoted by $\phi_{n\mathbf{q}}(\mathbf{r}, t)$. The overlap between these two states $\langle \phi_{n\mathbf{q}}(t) | \psi_{n\mathbf{q}}(t = 0) \rangle$ should be identically equal to unity at all times for the ideal case when the effective Hamiltonian exactly represents the evolution by the pulse sequence.

We arbitrarily choose a quasimomentum point $\mathbf{q} = (0.3, -0.2)k_{so}$ in the first Brillouin zone, and the eigenstate for the lowest band $n = 1$, for the case $\omega_0 = 32.3\omega_{so} = (2\pi) \times 9.3$ kHz and $\alpha = 1$, is calculated according to the method described in the last section. The absolute values of the overlap after evolving for 1 ms for $T = 40 \mu\text{s}$, $20 \mu\text{s}$ and $10 \mu\text{s}$, are respectively calculated to be 0.947, 0.984 and 0.995, indicating improved level of approximations with shorter periods.

The second method relies on wave packet evolution. For this case, an external trapping potential $V_{\text{trap}}(x, y) = \frac{1}{2}m(\omega_x^2 x^2 + \omega_y^2 y^2)$ is included into the Hamiltonian, and the initial state is prepared as a wave packet in the harmonic trap. Since the trap potential commutes with all the pulses, it is simply added into the effective Hamiltonian. The initial wave packet is then evolved respectively through the effective Hamiltonian and through the actually pulse sequence. We can then calculate some physical observables, e.g., population imbalance, by the corresponding time-dependent states, and compare their respective results. Figure S1 shows an example of this comparison. We can see that, they coincide with each other better for shorter evolution periods.

These studies indicate that for sufficiently short evolution periods, the effective Hamiltonian faithfully describes the evolution under the actual magnetic field pulse sequence. For the cases we discuss, $T = 10 \mu\text{s} \lesssim 1/\omega_0 = 17 \mu\text{s}$ is short enough to validate the effective Hamiltonian approximation.

Derivation of the emergent gauge fields

The evolution of a single-particle state is governed by the effective Hamiltonian according to

$$i\hbar \frac{\partial}{\partial t} |\Psi(\mathbf{r}, \mathbf{t})\rangle = H_{\text{eff}} |\Psi(\mathbf{r}, \mathbf{t})\rangle, \quad (\text{S20})$$

with H_{eff} given by Eq. (S16) for the spin 1/2 case. Expanded in the adiabatic basis, with corresponding center-of-mass wave functions labeled as $\psi_j(\mathbf{r}, \mathbf{t})$, the wave function takes the form

$$|\Psi(\mathbf{r}, \mathbf{t})\rangle = \sum_{j=1,2} \psi_j(\mathbf{r}, \mathbf{t}) |\chi_j(\mathbf{r})\rangle, \quad (\text{S21})$$

which when acted upon by the spin-dependent shift leads to

$$\left(\mathbf{p} - \frac{3}{16} \hbar k_{\text{so}} \boldsymbol{\sigma}_{\perp} \right) |\Psi(\mathbf{r}, \mathbf{t})\rangle = \sum_{l,j=1}^2 \left(\mathbf{p} \delta_{l,j} - \mathbf{A}_{lj} - \tilde{\mathbf{A}}_{lj} \right) \psi_j |\chi_l\rangle, \quad (\text{S22})$$

with

$$\begin{aligned} \mathbf{A}_{lj} &= i\hbar \langle \chi_l | \nabla \chi_j \rangle, \\ \tilde{\mathbf{A}}_{lj} &= \frac{3}{16} \hbar k_{\text{so}} \langle \chi_l | \boldsymbol{\sigma}_{\perp} | \chi_j \rangle. \end{aligned} \quad (\text{S23})$$

In the adiabatic limit $\omega_0 \gg \omega_{\text{so}}$, if the initial state is prepared in the dressed state $|\chi_1\rangle$, then the probability amplitude for the particle to be in the orthogonal state $|\chi_2\rangle$ remains zero at all time. Thus by projecting Eq. (S20) to the dressed state $|\chi_1\rangle$ and taking $\psi_2 = 0$, we get a closed equation for ψ_1

$$i\hbar \frac{\partial}{\partial t} \psi_1 = \left[\frac{1}{2m} (\mathbf{p} - \mathbf{A})^2 + \epsilon_0 + W \right] \psi_1, \quad (\text{S24})$$

where

$$\mathbf{A} \equiv \mathbf{A}_{11} + \tilde{\mathbf{A}}_{11} = i\hbar \langle \chi_1 | \nabla \chi_1 \rangle + \frac{3}{16} \hbar k_{\text{so}} \langle \chi_1 | \boldsymbol{\sigma}_{\perp} | \chi_1 \rangle, \quad (\text{S25})$$

is the geometric vector potential that couples to the center-of-mass motion, and

$$W = \frac{1}{2m} (\mathbf{A}_{12} \cdot \mathbf{A}_{21} + \tilde{\mathbf{A}}_{12} \cdot \tilde{\mathbf{A}}_{21} + \mathbf{A}_{12} \cdot \tilde{\mathbf{A}}_{21} + \tilde{\mathbf{A}}_{12} \cdot \mathbf{A}_{21}), \quad (\text{S26})$$

is the geometric scalar potential.

The resulting scalar potential consists of two terms. One is the adiabatic potential ϵ_0 , whose characteristic energy scale is $\hbar\omega_0$. The other is the geometric scalar potential W , which scales as $\hbar\omega_{\text{so}}$. Thus W makes a negligible contribution to the total scalar potential when compared to ϵ_0 , in the $\omega_0 \gg \omega_{\text{so}}$ limit. In Fig. S2, geometric potentials for $\alpha = 0, 0.72$, and 1 at $\omega_0 = 32.3\omega_{\text{so}}$ are shown. Compared to the corresponding adiabatic potentials shown respectively in Fig. 3(a) in the main text, with the corresponding potential (minima, maxima) in units of $\hbar\omega_{\text{so}}$ being $(-12.0, -4.0)$, $(-9.2, -6.7)$ and $(-10.0, -7.0)$ respectively, the geometric potentials only give small corrections to the final total scalar potentials. The qualitative understanding of the Haldane model as well as the topological phase transition enabled by our model is not affected by including these corrections.

If we take $\tilde{\mathbf{A}}_{lj} = 0$ in Eq. (S23), then the above results reduce to those reviewed by Dalibard *et al.* in Ref. [6], where momentum is not coupled to spin components in the original Hamiltonian, and the corresponding geometric potentials are $\mathbf{A} = i\hbar \langle \chi_1 | \nabla \chi_1 \rangle$ and $W = \mathbf{A}_{12} \cdot \mathbf{A}_{21}/2m = \hbar^2 |\langle \chi_1 | \nabla \chi_2 \rangle|^2/2m$.

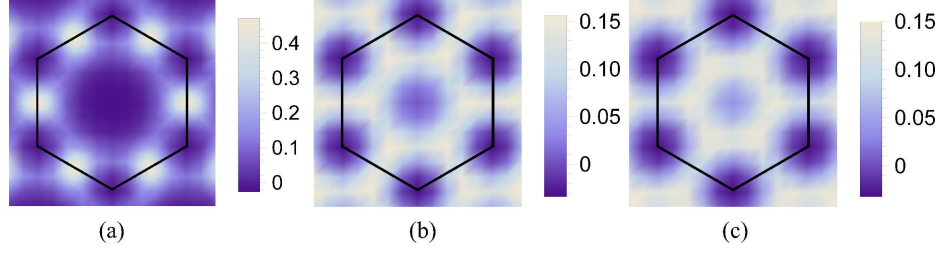


FIG. S2. The geometric scalar potentials W (in units of $\hbar\omega_{so}$) in Eq. (S26) at $\omega_0 = 32.3\omega_{so}$ for (a) $\alpha = 0$, (b) $\alpha = 0.72$, and (c) $\alpha = 1$.

Energy spectrum beyond the limit of adiabatic approximation

Although the discussion in the main text on the generation and understanding of the topological energy bands is based on models under the adiabatic as well as tight-binding approximation, the nontrivial topology of the energy bands is found to exist beyond these two approximations [22, 47]. As an example, we take $\alpha = 0.749$, and reduce the original ω_0 value by a factor of five to $\omega_0 = \frac{32.3}{5}\omega_{so} = (2\pi) \times 1.9$ kHz. The term of a Zeeman level is used instead of the adiabatic potential when the adiabatic approximation is not satisfied. At $\omega_0 = 6.46\omega_{so}$ with $\alpha = 0.749$, the (minima, maxima) of the two Zeeman levels of the magnetic lattice are respectively given by $(-1.84, -1.34)$ and $(1.34, 1.84)$ in units of $\hbar\omega_{so}$. The separation between the corresponding two levels is $2.68\hbar\omega_{so}$, and the lattice depth of the lower Zeeman level is a mere $0.5\hbar\omega_{so}$. As the energy scale for the spatial uniform term in Eq. (S16) is of order $\hbar\omega_{so}$, and SOC in this term can flip the spin, the lattice term does not dominate during the evolution; the adiabatic approximation fails for this case.

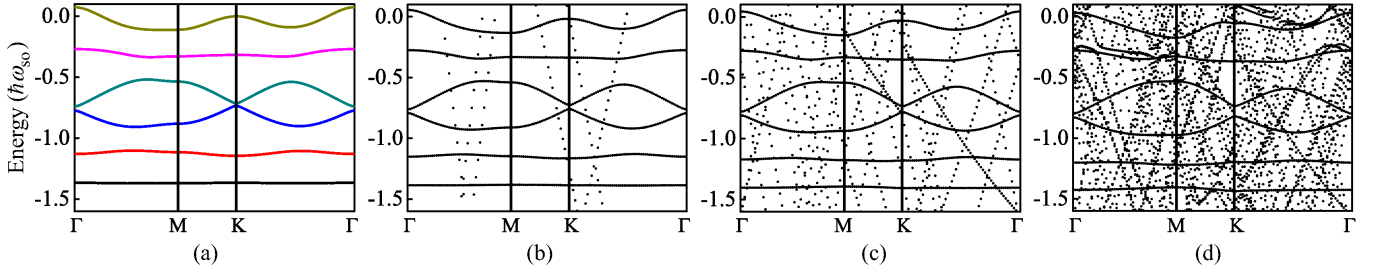


FIG. S3. The energy spectrum for our periodically driven model system at $\alpha = 0.749$ and $\omega_0 = 6.46\omega_{so} = (2\pi) \times 1.9$ kHz. (a) From the effective Hamiltonian Eq. (S16). (b-d) The quasienergies from solving the evolution operator in Eq. (S6) for (b) $T = 50\mu s$; (c) $T = 100\mu s$; and (d) $T = 200\mu s$.

The lowest six energy bands of the effective Hamiltonian for this case are shown in Fig. S3(a). Their Chern numbers are all found to be $C_n = 1$, which invalidates directly a tight-binding description, because the sum of Chern numbers for a set of tight-binding bands should be equal to zero. The band width for the lowest energy band is $0.0049\hbar\omega_{so}$, and the lowest band gap is $0.22\hbar\omega_{so}$, which gives a gap-over-width ratio of ~ 45 . Thus these Chern numbers for the lowest few bands resemble the ones for a charged particle in a magnetic field in a weak lattice background [49].

Next we discuss the validity of the effective Hamiltonian for this case. In previous subsection and in Fig. S1, we show the validity of the effective Hamiltonian for $\omega_0 = 32.3\omega_{so} = (2\pi) \times 9.3$ kHz, with respectively evolution periods $T = 10\mu s$, $20\mu s$, and $40\mu s$. In the present case of $\omega_0 = (2\pi) \times 1.9$ kHz, i.e., reduced by a factor of five, the suitable evolution period is expected to be increased by a similar factor. We can repeat the previous method by scanning state evolution period to illustrate the validity of adiabatic approximation, or alternatively, we can calculate the Floquet spectrum of quasienergies by evaluating the evolution operator Eq. (S6) directly for different evolution periods, with the results as shown in Fig. S3(b-d). We see that the spectrum of the quasienergies strongly resembles the one from the effective Hamiltonian at least for $T = 100\mu s$. The topological properties of the lowest energy band is expected to be preserved for $T = 200\mu s$, because no signature of band closing is found. For even larger evolution period, e.g. $T = 400\mu s$, the quasienergies for the lower energy bands are found to be smeared out due to the wrapping of the higher Floquet sectors with quasienergies at multiples of $2\pi\hbar/T$. Thus we conclude the suitable evolution period required for the validity of the effective Hamiltonian approximation is of the order of $\sim 100\mu s$ for the present choice of $\omega_0 = (2\pi) \times 1.9$ kHz.

Adiabatic preparation of the ground state

As is verified in the previous sections, one can use the effective Hamiltonian Eq. (S16) to describe the state evolution under the pulse sequence for short evolution periods. In this section, we describe how can the ground state of the effective Hamiltonian Eq. (S16) be reached through an adiabatic loading approach. For a non-interacting many-body fermionic system, the ability of preparing its ground state is essentially equivalent to the statement that all the (single-particle) eigenstates in the lowest energy band of H_{eff} in Eq. (S16) can be reached appropriately.

As shown in the main text, one complete cycle of the evolution period consists of four subperiods. To prepare the ground state, we will keep the fourth subperiod intact, while adiabatically ramp up (a) the strength of the gradient pulses in N_a complete cycles and then (b) the bias magnetic field for the first three subperiods in N_b complete cycles.

A quantitative analysis is provided as follows. We first introduce an auxiliary Hamiltonian

$$\mathcal{H}(\kappa, \gamma) = \frac{\mathbf{p}^2}{2m} - \frac{3\hbar k_{\text{so}}}{16m} \kappa (p_x \sigma_x + p_y \sigma_y) - \frac{\alpha}{8} \hbar \omega_0 \sigma_z + \frac{\gamma}{8} \hbar \omega_0 \mathbf{M} \cdot \boldsymbol{\sigma}, \quad (\text{S27})$$

where the three components of the \mathbf{M} vector are respectively $M_x = -\sum_j \sin(k_{\text{so}} r_{\theta_j}) \sin(\theta_j)$, $M_y = \sum_j \sin(k_{\text{so}} r_{\theta_j}) \cos(\theta_j)$, and $M_z = \sum_j \cos(k_{\text{so}} r_{\theta_j})$. The effective Hamiltonian before the aforementioned ramping process is $\mathcal{H}(\kappa = 0, \gamma = 0)$; the effective Hamiltonian at the end of the ramping stage (a) is $\mathcal{H}(\kappa = 1, \gamma = 0)$; and the effective Hamiltonian after ramping stage (b) is $\mathcal{H}(\kappa = 1, \gamma = 1)$, which recovers the effective Hamiltonian H_{eff} in Eq. (S16).

As a proof-of-principal illustration, suppose the initial state for the ramping stage (a) is prepared as a plain wave in the spin up state

$$\langle \mathbf{r} | \psi_{\text{ini},a} \rangle = \exp(i\mathbf{p} \cdot \mathbf{r}/\hbar) \begin{pmatrix} 1 \\ 0 \end{pmatrix}, \quad (\text{S28})$$

which is the eigenstate of $\mathcal{H}(\kappa = 0, \gamma = 0)$ in the lower branch (we always consider positive α). The target state for the ramping stage (a) is the corresponding eigenstate of $\mathcal{H}(\kappa = 1, \gamma = 0)$:

$$\langle \mathbf{r} | \psi_{\text{tar},a} \rangle = \exp(i\mathbf{p} \cdot \mathbf{r}/\hbar) \begin{pmatrix} \alpha \hbar \omega_0 + \sqrt{\frac{9\hbar \omega_{\text{so}} \mathbf{p}^2}{2m} + (\alpha \hbar \omega_0)^2} \\ 3\omega_{\text{so}}(p_x + ip_y)/k_{\text{so}} \end{pmatrix}. \quad (\text{S29})$$

Here the spin state is not normalized. We denote the wavefunction during stage (a) under the pulse sequence as $|\phi_{\mathbf{p}}(t)\rangle$. The fidelity between this state and the target state is then given by

$$F_{\mathbf{p}}(t) = \left| \langle \psi_{\text{tar},a} | \phi_{\mathbf{p}}(t) \rangle \right|^2. \quad (\text{S30})$$

We notice that, the initial fidelity for stage (a) is

$$F_{\mathbf{p}}(t=0) = \left| \langle \psi_{\text{tar},a} | \psi_{\text{ini},a} \rangle \right|^2 = \frac{\left(\alpha \hbar \omega_0 + \sqrt{9\hbar \omega_{\text{so}} \mathbf{p}^2 / 2m + (\alpha \hbar \omega_0)^2} \right)^2}{\left(\alpha \hbar \omega_0 + \sqrt{9\hbar \omega_{\text{so}} \mathbf{p}^2 / 2m + (\alpha \hbar \omega_0)^2} \right)^2 + 9\hbar \omega_{\text{so}} \mathbf{p}^2 / 2m}, \quad (\text{S31})$$

which is close to unity for small momentums and large $\alpha \omega_0 / \omega_{\text{so}}$. For instance, for the momentum point $\mathbf{p} = (1, 1) \hbar k_{\text{so}}$ in the lower energy branch, with $\omega_0 = 32.3 \omega_{\text{so}} = (2\pi) \times 9.3 \text{ kHz}$ and $\alpha = 1$, we get $F_{\mathbf{p}}(t=0) = 99.57\%$. After linearly ramping up κ from zero to one in $N_a = 40$ cycles with period $T = 10 \mu\text{s}$, the final fidelity is numerically found to be $F_{\mathbf{p}}(t = N_a T) = 1 - 4.3 \times 10^{-5}$. This shows that the low energy eigenstates of $\mathcal{H}(\kappa = 1, \gamma = 0)$ can be reached reliably.

We then consider the ramping process for stage (b). We choose the initial state for this stage as the lowest eigenstates of $\mathcal{H}(\kappa = 1, \gamma = 10^{-6})$. The vanishingly small lattice term $10^{-6} \times \frac{1}{8} \hbar \omega_0 \mathbf{M} \cdot \boldsymbol{\sigma}$ introduced in our numerical simulation accounts for the effect of the Bragg reflections at the edges of the first Brillouin zone, which turns the good quantum number from momentum (denoted as \mathbf{p}) to quasimomentum (denoted as \mathbf{q}) restricted in the first Brillouin zone [49]. The fidelity between the target state $|\psi_{1\mathbf{q}}\rangle$ [i.e., eigenstate of Eq. (S16) with the form of Eq. (S17) with band index $n = 1$] and the time-dependent state $|\phi_{\mathbf{q}}(t)\rangle$ evolved by pulse sequence with increased magnetic lattice strength (which is proportional to γ) is defined as:

$$F_{\mathbf{q}}(t) = \left| \langle \psi_{1\mathbf{q}} | \phi_{\mathbf{q}}(t) \rangle \right|^2. \quad (\text{S32})$$

We suggest ramping up the strength of the magnetic lattice as a tangent function (rather than a linear one), which corresponds to a time-dependent γ function with the form

$$\gamma(t) = \frac{\tan[\eta\pi t / (2N_b T)]}{\tan(\eta\pi/2)}, \quad (\text{S33})$$

where the parameter η is taken as 0.975. The typical results for the time-dependent fidelity functions for different quasimomentums, together with the $\gamma(t)$ function, are shown in Fig. S4. As can be seen in this figure, the fidelities after ramping up the magnetic lattice approach unity for all tested quasimomentum points. We thus conclude that the eigenstates in the lowest energy band of the effective Hamiltonian H_{eff} in Eq. (S16) can be prepared appropriately through the adiabatic approach we propose.

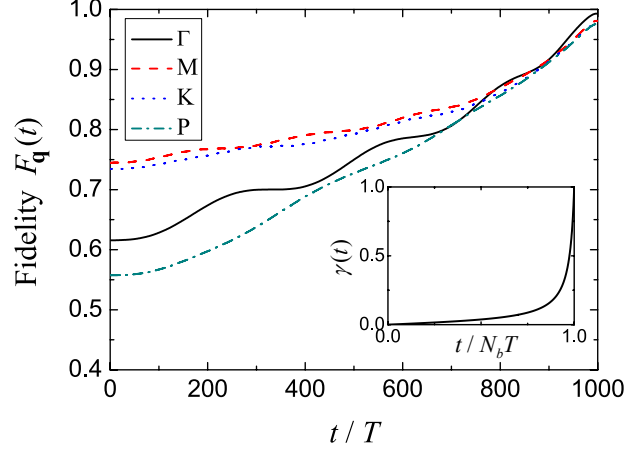


FIG. S4. The time-dependent fidelities for selected quasimomentum points in the first Brillouin zone. Here in the legend, P stands for the result for the quasimomentum point $\mathbf{q} = (0.3, -0.2)k_{\text{so}}$. The strength of the magnetic lattice is ramped up as a tangent function (the inset) in $N_b = 1000$ cycles. The parameters for the system are the following: $\omega_0 = 32.3\omega_{\text{so}} = (2\pi) \times 9.3$ kHz, $\alpha = 1$ and $T = 10 \mu\text{s}$.